2024-03

FABRICATING POROUS METAL STRUCTURES CAPABLE OF CAPILLARY ACTION THROUGH ADDITIVE MANUFACTURING

Misch, Kristofer I.

Monterey, CA; Naval Postgraduate School

NAVAL POSTGRADUATE SCHOOL

MONTEREY, CALIFORNIA

THESIS

FABRICATING POROUS METAL STRUCTURES CAPABLE OF CAPILLARY ACTION THROUGH ADDITIVE MANUFACTURING

by

Kristofer I. Misch

March 2024

Thesis Advisor: Ibrahim E. Gunduz
Second Reader: Christopher C. Curran

THIS PAGE INTENTIONALLY LEFT BLANK

REPORT DOCUMENTATION PAGE	*Form Approved OMB No. 0704-0188*

1. AGENCY USE ONLY *(Leave blank)*	**2. REPORT DATE** March 2024	**3. REPORT TYPE AND DATES COVERED** Master's thesis

4. TITLE AND SUBTITLE
FABRICATING POROUS METAL STRUCTURES CAPABLE OF CAPILLARY ACTION THROUGH ADDITIVE MANUFACTURING

5. FUNDING NUMBERS

6. AUTHOR(S) Kristofer I. Misch

7. PERFORMING ORGANIZATION NAME(S) AND ADDRESS(ES)
Naval Postgraduate School
Monterey, CA 93943-5000

8. PERFORMING ORGANIZATION REPORT NUMBER

9. SPONSORING / MONITORING AGENCY NAME(S) AND ADDRESS(ES)
N/A

10. SPONSORING / MONITORING AGENCY REPORT NUMBER

11. SUPPLEMENTARY NOTES The views expressed in this thesis are those of the author and do not reflect the official policy or position of the Department of Defense or the U.S. Government.

12a. DISTRIBUTION / AVAILABILITY STATEMENT
Approved for public release. Distribution is unlimited.

12b. DISTRIBUTION CODE
A

13. ABSTRACT (maximum 200 words)

The low-density and corrosion resistance of aluminum alloys make them useful for heat pipes in aerospace applications where heavier metals like copper and steel would be less desirable. This can be used for rapid, compact cooling of heat generating systems. However, traditional methods of manufacturing porous wicks can prove ineffective for complicated geometries, as fine aluminum wire can be difficult to produce and weave into a mesh, and sintering Al powder may leave impurities. Through liquid metal printing, a porous Al wick can be made within a fully dense structural element that is capable of capillary action without the need of additional processing. Different levels of porosity can be achieved by controlling the droplet size and jetting frequency in liquid metal printing, allowing the wick to be fine-tuned to strike the correct balance of capillary force and wick permeability.

Using an ElemX metal 3D printer, we were able to 3D print wick samples made of Al-4008 alloy with cross-sectional porosities of up to 31.5%, as well as wicks that could transport 0.4734 g/min of water. The project also confirms the capability of printing multiple structures on top of one another to produce composite assemblies of different densities as well as complicated geometries. A 3-point flexure test was conducted on solid aluminum beams, porous beams, and a composite hollow structure with a solid shell and porous wick able to withstand flexural stresses of up to 290 MPa before failure.

14. SUBJECT TERMS
3D printing, additive manufacturing, liquid metal printing, fused filament fabrication, heat pipes, capillary action

15. NUMBER OF PAGES
65

16. PRICE CODE

17. SECURITY CLASSIFICATION OF REPORT	**18. SECURITY CLASSIFICATION OF THIS PAGE**	**19. SECURITY CLASSIFICATION OF ABSTRACT**	**20. LIMITATION OF ABSTRACT**
Unclassified	Unclassified	Unclassified	UU

NSN 7540-01-280-5500

Standard Form 298 (Rev. 2-89)
Prescribed by ANSI Std. 239-18

THIS PAGE INTENTIONALLY LEFT BLANK

Approved for public release. Distribution is unlimited.

FABRICATING POROUS METAL STRUCTURES CAPABLE OF CAPILLARY ACTION THROUGH ADDITIVE MANUFACTURING

Kristofer I. Misch
Lieutenant, United States Navy
BS, United States Naval Academy, 2017

Submitted in partial fulfillment of the
requirements for the degree of

MASTER OF SCIENCE IN MECHANICAL ENGINEERING

from the

NAVAL POSTGRADUATE SCHOOL
March 2024

Approved by: Ibrahim E. Gunduz
Advisor

Christopher C. Curran
Second Reader

Brian S. Bingham
Chair, Department of Mechanical and Aerospace Engineering

THIS PAGE INTENTIONALLY LEFT BLANK

ABSTRACT

The low-density and corrosion resistance of aluminum alloys make them useful for heat pipes in aerospace applications where heavier metals like copper and steel would be less desirable. This can be used for rapid, compact cooling of heat generating systems. However, traditional methods of manufacturing porous wicks can prove ineffective for complicated geometries, as fine aluminum wire can be difficult to produce and weave into a mesh, and sintering Al powder may leave impurities. Through liquid metal printing, a porous Al wick can be made within a fully dense structural element that is capable of capillary action without the need of additional processing. Different levels of porosity can be achieved by controlling the droplet size and jetting frequency in liquid metal printing, allowing the wick to be fine-tuned to strike the correct balance of capillary force and wick permeability.

Using an ElemX metal 3D printer, we were able to 3D print wick samples made of Al-4008 alloy with cross-sectional porosities of up to 31.5%, as well as wicks that could transport 0.4734 g/min of water. The project also confirms the capability of printing multiple structures on top of one another to produce composite assemblies of different densities as well as complicated geometries. A 3-point flexure test was conducted on solid aluminum beams, porous beams, and a composite hollow structure with a solid shell and porous wick able to withstand flexural stresses of up to 290 MPa before failure.

THIS PAGE INTENTIONALLY LEFT BLANK

TABLE OF CONTENTS

THIS PAGE INTENTIONALLY LEFT BLANK

LIST OF FIGURES

THIS PAGE INTENTIONALLY LEFT BLANK

LIST OF TABLES

THIS PAGE INTENTIONALLY LEFT BLANK

LIST OF ACRONYMS AND ABBREVIATIONS

3D	3 Dimensional
AGHP	Axially Grooved Heat Pipe
AM	Additive Manufacturing
ASTM	American Society for Testing and Materials
CAD	Computer Aided Design
CNC	Computer-Numeric-Controlled
CRADA	Cooperative Research and Development Agreement
DED	Directed Energy Deposition
DOD	Department of Defense
HMI	Human Machine Interface
JF	Jetting Frequency
LMJP	Liquid Metal Jet Printing
MPF	Main Program File
NASA	National Aeronautics and Space Agency
PBF	Powder Bed Fusion
PHT	Pulse High Time
SLS	Selective Laser Sintering
SLM	Selective Laser Melting
STL	Standard Tessellation Language

THIS PAGE INTENTIONALLY LEFT BLANK

ACKNOWLEDGMENTS

I would first like to thank my amazing wife, Kayla Mahoney-Misch, for supporting me throughout this whole endeavor. You gave me the motivation to continue when I wanted to tear my hair out, and I do not know if I could have done this without knowing I had you waiting at home.

I would also like to thank my advisor, Dr. Emre Gunduz, for helping to guide me through the project and show which avenues to explore, as well as giving me the necessary tools to succeed. In addition, I would like to express my gratitude to ElemX technician Rogelio Jacobomartinez, who stuck around with the patience of a saint during the printing process to ensure proper part quality, machine start-up/shutdown, and troubleshooting. If I had to do all of that myself, I would not have gotten half as far as I did. And last but certainly not least, a thank you to my fellow collaborators ENS Victor Wang and LT Zach Vrtis, who taught me how to use the ElemX machine and provided a starting point from which to begin my thesis work, as well as giving parallel feedback as we did our own projects.

THIS PAGE INTENTIONALLY LEFT BLANK

I. INTRODUCTION

A. MOTIVATION

The Additive Manufacturing industry has seen a significant amount of focus in recent years, especially with regards to the new possibilities for its applications. The Department of Defense and NASA have a vested interest in the progression of Additive Manufacturing [1], and the Naval Postgraduate School has made many partnerships to help facilitate this. One such partnership explores the capabilities of the Additec ElemX 3D Printer (formerly owned by Xerox) through a Cooperative Research and Development Agreement (CRADA).

Through the AM method used by the ElemX printer, new prospects for existing technology have been explored. It was discovered in previous tests conducted with ENS Victor Wang that it is possible to print objects of varying densities by changing the parameters of the printer [2]. This opens the possibility that objects printed with different densities could be porous enough to work as a medium to transport liquid. This means that discontinuities and voids, which were often points of structural weakness, can now be integral to the composition of a design.

One such application is in printing heat pipes. The lightweight and corrosion-resistant properties of aluminum make aluminum heat pipes useful for aerospace applications where heavier metals like copper and steel would be less desirable [3]. Through liquid metal aluminum 3D printing, a porous aluminum wick can be fabricated that is capable of capillary action.

B. OBJECTIVES

This report builds on previous findings to discover applications of aluminum parts with varying density [2]. The aim of this project is to develop a composite aluminum assembly combining both solid and porous aluminum structures by adjusting the parameters available on the ElemX metal 3D printer. Ideally, it should also be capable of capillary action. We shall also explore the potential of using the composite assemblies as support structures by observing yield stress.

By observing how different factors interact with one another, we can better optimize the process for their unique applications. Different levels of porosity are achieved by controlling the droplet size and jetting frequency of the machine, allowing the wick to be fine-tuned to strike the correct balance of capillary force and wick permeability. In addition, the process will also be judged by how efficient it is and how consistently it can produce proper results. Finally, we will also characterize the strength of the materials when subjected to loading.

II. BACKGROUND

A. ADDITIVE MANUFACTURING

Additive Manufacturing (AM) is a process of bonding materials to make items using the data of a 3-D model. Also known as 3D printing, AM allows for the objects to be designed in a CAD software, uploaded to the machine, and then "printed" using techniques unique to their method. In contrast to many subtractive manufacturing technologies, AM techniques are good for minimizing waste by using just the material required to make an object along with any necessary supports or rafts.

There are several methods that exist for 3D printing metals. Some of the more common ones involve the use of powders as a medium, such as with Powder Bed Fusion (PBF) or Directed Energy Deposition (DED). Metal wire can also be used as a material source for DED and Liquid Metal Jet Printing (LMJP). The method used for this study is a type of LMJP that uses MagnetoJet Technology, visualized in Figure 1.

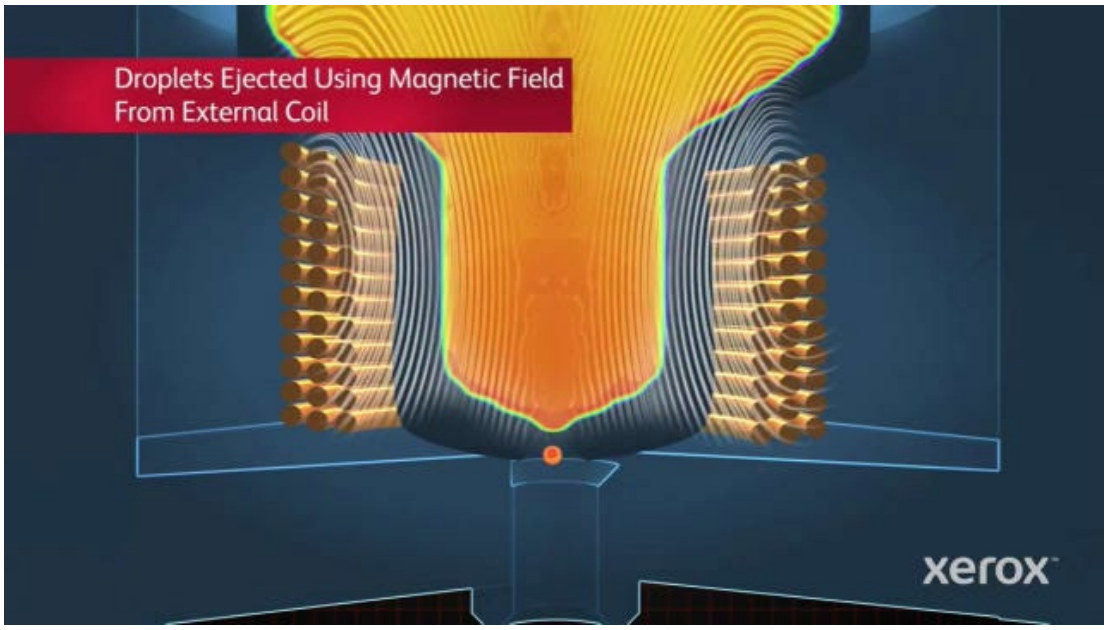

Figure 1. MagnetoJet Technology. Source: [4].

The machine used is an Additec ElemX 3D Printer (formerly owned by Xerox), which is a molten aluminum three-dimensional additive printer [5]. Aluminum wire is melted using a resistive heater located in the print head assembly and fed into a refractory pump that holds it at or above the melting temperature. The molten aluminum is then ejected using a pulsed magnetic field generated by an electromagnetic coil, focusing the melted metal through a 500 μm graphite nozzle so it is ejected as a jet of droplets. The molten aluminum is deposited onto a heated bronze bed located directly below it, as depicted in Figure 2. Utilizing a CNC motion system, the print bed moves along the X and Y axes for horizontal movement, while the print head moves vertically along the Z-axis.

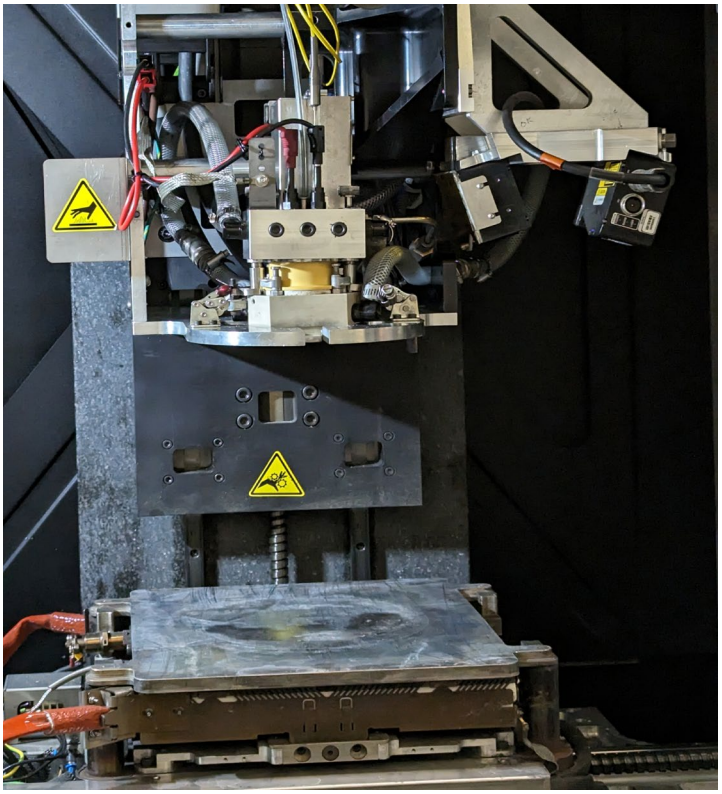

Figure 2. ElemX Printhead and Heated Bed.

As the machine runs on G-Code, any models must be uploaded into the ElemX slicing software in preparation for uploading it into the machine. The software accepts a wide range of file types from STL files to SolidWorks parts.

The machine is controlled through a Human-Machine Interface, or HMI, consisting of a touchscreen display, a standard QWERTY keyboard, and an Operator Button Panel. The touchscreen display, depicted in Figure 3, is the primary interface for users, providing the user with a variety of menus that one may use to control and monitor the printer. The menus are navigated using the tabs at the bottom of the display. In the order they are presented at the bottom of the screen, there is a menu for Recipes, Thermal Controls, Metal Controls, Overview, Build Plate Load/Unload—Process Shutdown, Operate, User Diagnostics, Trends, and Service Diagnostics. There is also a tab at the very end to exit the program.

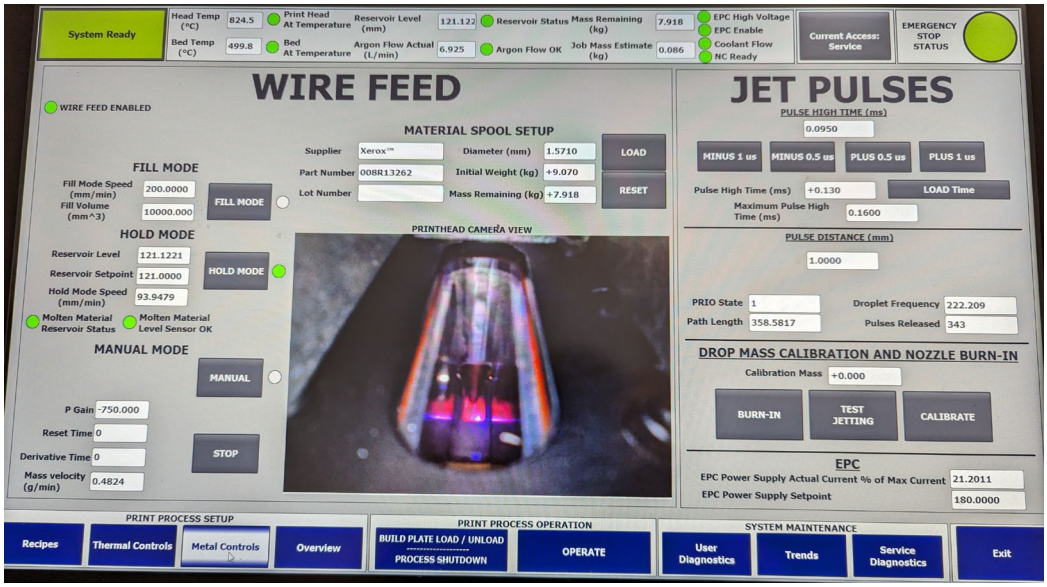

Figure 3. HMI Menu for Metal Controls.

The Operator Button Panel controls many of the factors inherent to the actual machine such as coolant, Argon gas flow, and wire feed. The jetting frequency of the machine is also controlled from here, using the knobs shown in Figure 4.

Figure 4. Operator Button Panel.

1. Controllable Factors

In order to fine-tune the process of producing a usable wick, the right combination of factors is needed. The following variables are capable of being changed:

- Pulse High Time (PHT): Changing the coil pulse high time allows adjustments to the size of the drop mass. Raising PHT increases the size of each drop while lowering the PHT decreases the size. Since the printer still follows its programmed path, the smaller drop masses end up with more spacing between each drop than originally intended. This can create a porous structure when operating a small enough drop size but will also consequently result in a product that is shorter than originally designed. PHT can be adjusted during the printing process, meaning that a single print can have a gradient of porosity.

- Jetting Frequency (JF): Also known as the Axes Feed Rate, changing the jetting frequency controls the machine's rate of deposition and the movement speed of the X, Y and Z axes. The control dial for JF displays percentages, with the recommended setting being 100%. The percentages correspond to a frequency in Hz equal to 5 times the percentage (e.g., 30% corresponds to 150 Hz). Lowering the JF helps when printing at lower PHTs, as not only does it allow for a more stable stream, but the slower speeds allow for better shape retention as the droplets do not spread and fill gaps [6]. This will be at the cost of longer print times, providing more chances of nozzle blockage as the slower speeds allow the nozzle to cool. Furthermore, the jetting frequency cannot be changed mid-print.

- Print Optimization: The ElemX comes with a built-in setting for the printer meant to automatically apply corrections by scanning the print every few layers. The option can be turned off before starting a print. While it can be an excellent tool for ensuring a printed object maintains its designed structure, it may abort a given part if it determines it can no longer compensate for inaccuracies. In addition, print optimization will not work when printing on top of another print, meaning that any sample must be a single continuous object rather than an assembly.

- Model Geometry: The shape and size of the model can be adjusted to compensate for issues discovered during the printing process, such as a loss in height as a result of the parameter changes or improper overhang angles.

- Slicer Settings: Several settings present in the slicing software can be configured to compensate for the effects of changing other factors. For example, by changing the infill method to use perimeter shell infills, we can make it so the interior geometry does not shrink as much after altering the PHT. However, this means that the distribution of porosity may be more uniform rather than randomly distributed.

2. Limitations

Despite its various uses, 3-D printing is still limited by several constraints. Some limitations are listed in the ElemX Design Guide [7] but can change with the parameters. The suggested size of any features is 3 mm, as any less may result in a loss of fidelity. Overhang angles are recommended to be 50 degrees or greater, as the layers may not properly adhere at smaller angles and result in sagging or loss of features if supports are not provided. Figure 5 shows that when printing at lower settings, the acceptable overhang angle changes drastically. This increases the difficulty in trying to design a circumferential wick, as it cannot maintain its intended shape without drastic changes to the angle.

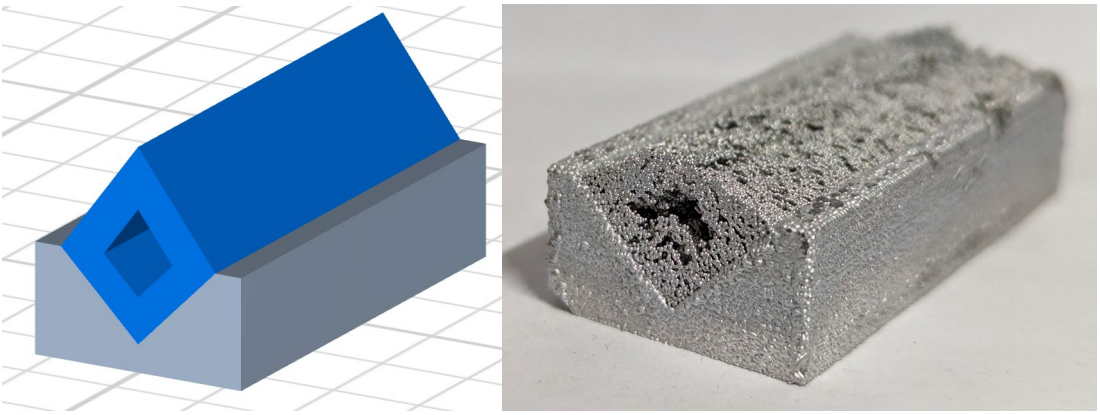

Figure 5. Hollow Wick Designed in SolidWorks: (Left). Resulting Model: (Right).

From prior tests, we found that when printing two objects concentrically, the second object printed would be limited by the height of the first object. If printing on the same Z-plane, the second print would be limited by about 8 mm [2]. The Z-plane may be adjusted, but this may result in inaccurate layers and binding issues. If the print head is too high above the build plate, the molten particles may end up cooling down before they reach the bottom, resulting in improper fusion, or even beads of aluminum bouncing off the build plate.

3. Al-4008

The ElemX printer is designed with Al-4008 as its primary alloy. Also known as Al-A356, the alloy is conventionally used as a welding wire [8]. It consists of primarily Aluminum, with 7% Silicon, 0.4% Magnesium, and 0.08% Titanium and Iron, with some other trace elements. It is widely used for casting [9]. Table 1 depicts the physical properties of this alloy.

Table 1. Al-4008 Properties. Adapted from [8].

Melting Range (°C)	550-615
Density (g/cm^3)	2.66
Hardness (HV)	60-105

B. HEAT PIPES

Heat pipes are passive thermal regulation devices that can transport heat against gravity through an evaporation-condensation cycle [10]. They require no external pumps and are self-regulating, meaning no external power or flow control devices are needed for the device to work as intended. The type of heat pipe that is the focus of this study is a capillary heat pipe, depicted in Figure 6. Capillary heat pipes consist of three basic components: the container, the capillary structure or wick, and the working fluid.

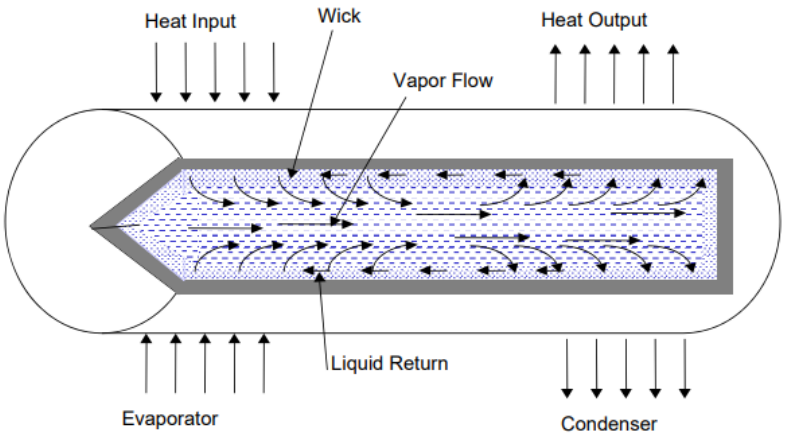

Figure 6. Basic Heat Pipe Composition. Source: [11].

The container is the outer shell of the pipe that prevents any fluid from escaping while also typically being the medium in direct contact with the heat source and heat sink. The container is usually made of metal due to their inherently high heat conductivity. The three most common metals used are steel, copper and aluminum [3]. While most heat pipe containers are cylindrical or rectangular, the same techniques can be applied to specific applications requiring special geometries. For example, some heat pipes can be designed for use in the leading edges of supersonic aircraft and must be customized to properly regulate the space [12].

The wick is the component that assists the movement of liquid throughout the pipe using capillary action. While it is possible to use a different material from the container, wicks of the same material prevent issues that could arise from differences in chemical and physical properties. Most variation in cross-sectional geometry is seen with the wick. The most basic versions have a homogenous, circumferential wick consisting of sintered powder or fine woven mesh of metallic wire [10]. Some more intricate heat pipes may incorporate an arterial wick structure, where an open channel enclosed by the wick material provides fluid a fast way to travel insulated from vapor. While unconventional, some heat pipes can be designed to be unidirectional, with the wick along one side of the container for specialized heat transfer [13].

Many aluminum heat pipes utilized in aerospace capacities are axial grooved heat pipes (AGHP), using small, narrow grooves to facilitate capillary action. AGHPs are typically made using metal extrusion, though they are also well suited for most methods of metal 3D printing such as selective laser melting technology due to the homogeneity of the pipe [14]. This works well for systems that are not subjected to large gravitational forces, but function less effectively in environments closer to earth. In addition, they are less efficient at heat transport than porous wicks.

To function with a greater amount of capillary force, many traditional heat pipes utilize either a fine wire mesh or sintered powder to fabricate a porous structure. A wire mesh is more prevalent in copper or steel heat pipes, as it is difficult to both produce and weave together aluminum wire fine enough to facilitate capillary action. Sintered aluminum powder can produce a porous structure that can function as a working wick

[15]. Current sintering processes can introduce oxides when done in an open environment or can involve spacing materials that are then chemically removed. By using LMJP to layer molten aluminum droplets, we should be able to achieve the same result accomplished with sintering with the added benefit of the argon shielding inherent in the machine to help protect the parts from oxidation.

Larger pore sizes allow for greater volumes of liquid to be transferred, while smaller pores allow for greater capillary forces [3]. As we are making a capillary wick, we need to determine whether the printer is capable of printing a structure capable of capillary action while still being able to transport fluid. To calculate capillary pressure capability, we can use the following equation [3]:

$$\Delta P_{cap,\max} = \frac{2\sigma\cos\theta}{R_p}.$$

Per the equation, σ is Surface Tension, R_p is the radius of the pore, and θ is the contact angle.

THIS PAGE INTENTIONALLY LEFT BLANK

III. PROCEDURE

A. TEST SETTINGS

Several samples were printed to observe the changes that came with altering the print settings. The first batch were designed with a combination of simple geometries, with a 14x50x3 rectangular base and a rounded wick as shown in Figure 7. The small size of the part allows for multiple samples to be printed on the bed before removal. The distinctness of the two parts allowed one to more easily see any issues that came up between the wick and the base during the printing process.

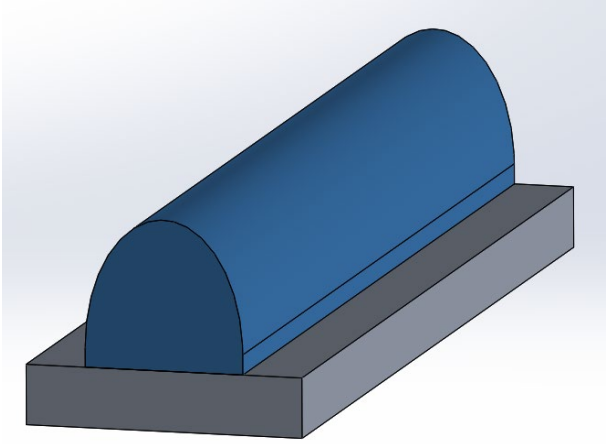

Figure 7. CAD Design of Model, Made in SolidWorks 2020.

All the bases were printed with the standard recommended settings: a PHT of 0.130 ms and a JF of 100%. Figures 8–13 show the first six samples, which were modelled as a single part. The PHT was manually changed upon reaching layer 12, where the base transitioned to the wick. This required a user to be present to change the settings at the correct time, as altering it any earlier would result in a porous base and any later would result in a wick with not enough porosity. Changes to Jetting Frequency would also not be possible during the transition from base to wick. However, having the print be a single part meant that the wick was more directly adhered to the base, and there would be little chance of the wick being incorrectly offset from the base. It also allows users to

utilize the Print Optimization function for the whole print, which helps to maintain shape. Using the Print Optimization function also adds another aspect of failure, though, as the machine will abort the program if the settings are being changed during a layer scan in addition to the reasons listed in section [II.A.1].

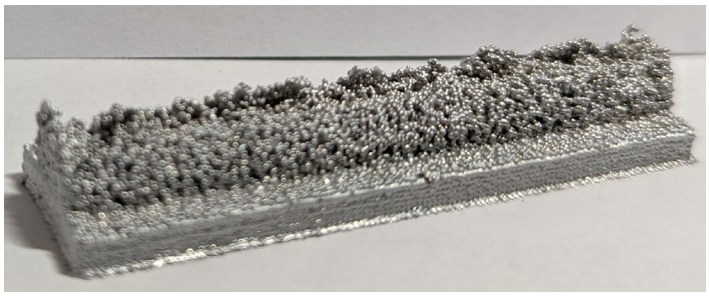

Figure 8. Sample 1: Wick PHT 0.100 ms, Jetting Frequency: 100%, Print Optimization: Off.

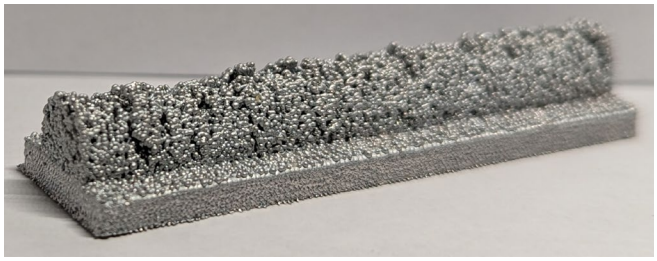

Figure 9. Sample 2: Wick PHT 0.100 ms, Jetting Frequency: 100%, Print Optimization: On.

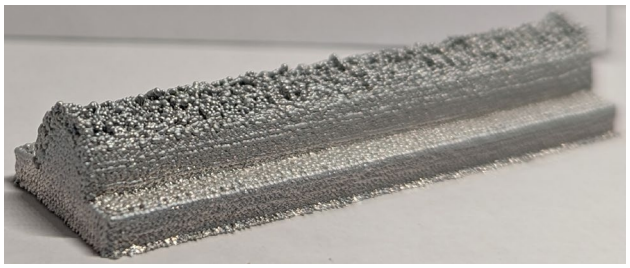

Figure 10. Sample 3: Wick PHT 0.125-0.100 ms (Gradient), Jetting Frequency: 100%, Print Optimization: Off.

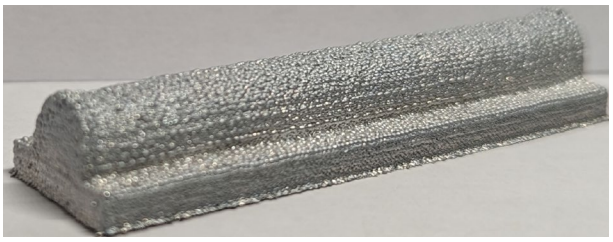

Figure 11. Sample 4: Wick PHT 0.115 ms, Jetting Frequency: 100%, Print Optimization: Off.

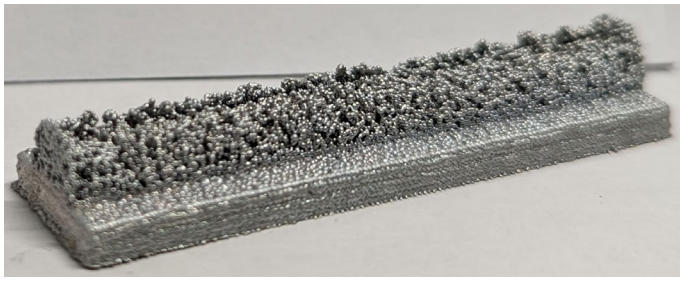

Figure 12. Sample 5: Wick PHT 0.090 ms, Jetting Frequency: 100%, Print Optimization: On.

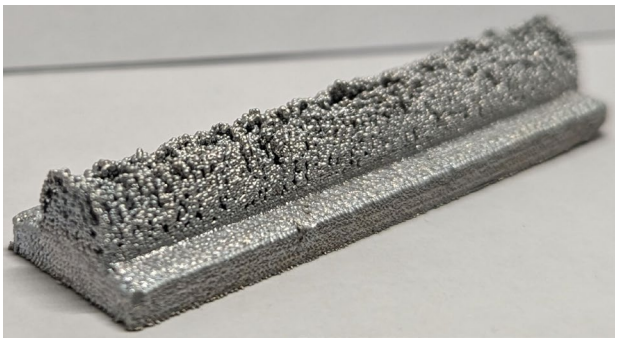

Figure 13. Sample 6: Wick PHT 0.095 ms, Jetting Frequency: 100%, Print Optimization: On.

At 100% jetting frequency, one of the biggest issues that we saw was that many of the samples would print with an uneven upper surface. The sides would form a shell growing over the interior, leaving a small overhang with a recess in the center. Print Optimization corrected this to some degree, but still left a small overhang on samples printed at lower PHTs.

Figures 14–23 show the next 12 samples, which use the same basic geometry but have the base and wick designed as two separate parts. This allows changes to jetting frequency between parts, while also not requiring a user to manually time the change in PHT as it can be done before the wick is started. Print optimization could not be applied to the wick as the machine will usually respond with a fatal error upon attempting to print on top of another object, though it can be used for the base.

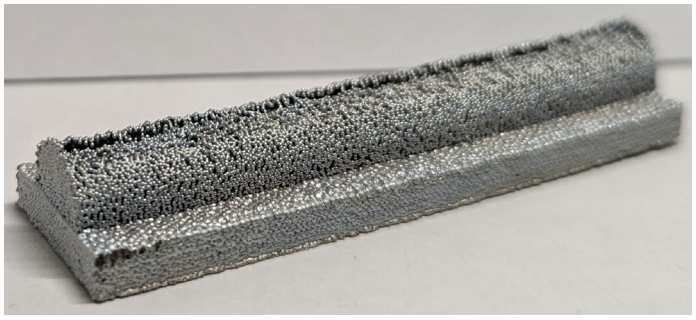

Figure 14. Sample 7: Wick PHT 0.095 ms, Jetting Frequency: 10%, Print Optimization: Off, Infill Type: Standard.

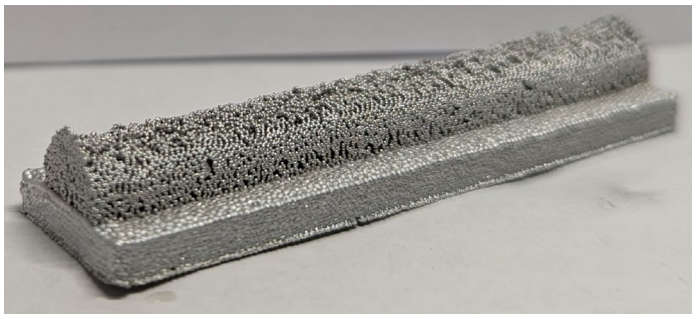

Figure 15. Sample 8: Wick PHT 0.095 ms, Jetting Frequency: 10%, Print Optimization: Off, Infill Type: Shell.

Between Samples 7 and 8, the infill type was changed from the standard infill to one using perimeter shells. This means that the interior was built using the same settings as the outer perimeter, ensuring less height difference between the sides of the print and the center. The result was a more uniform distribution throughout the sample.

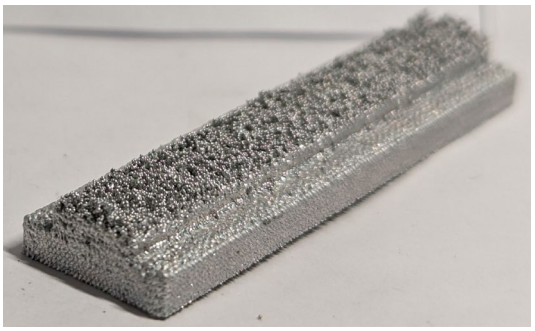

Figure 16. Sample 9: Wick PHT 0.085 ms, Jetting Frequency: 40%, Print Optimization: Off, Infill Type: Shell.

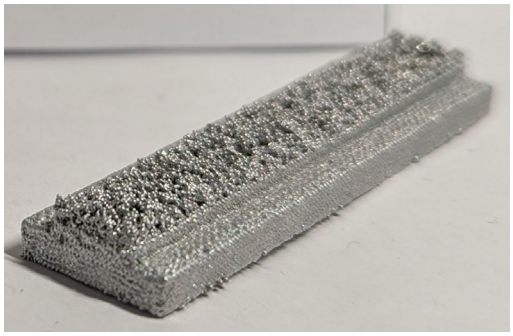

Figure 17. Sample 10: Wick PHT 0.100 ms, Jetting Frequency: 40%, Print Optimization: Off, Infill Type: Shell.

The wicks for Samples 9 and 10 were started at a PHT of 0.130 ms and then dropped to their final respective PHT. This was done to ensure the nozzle was at an appropriate temperature before continuing with the rest of the wick, but ultimately did not improve results. As we can see in both Figure 16 and Figure 17, changing the settings while at a lower frequency had detrimental effects on the overall integrity of the wick.

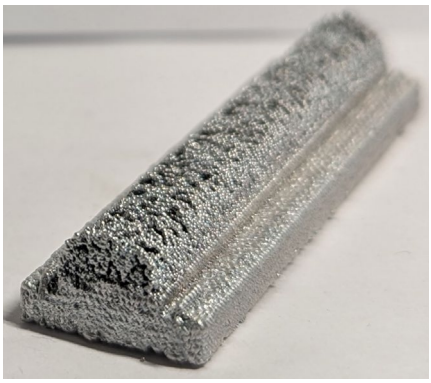

Figure 18. Sample 11: Wick PHT 0.100 ms, Jetting Frequency: 20%, Print Optimization: Off, Infill Type: Shell.

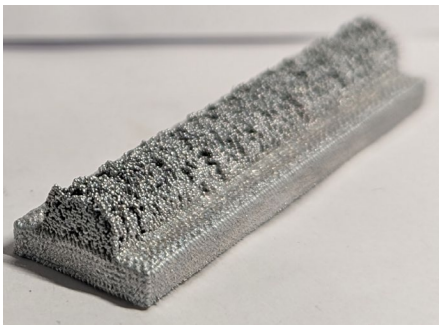

Figure 19. Sample 12: Wick PHT 0.095 ms, Jetting Frequency: 20%, Print Optimization: Off, Infill Type: Shell.

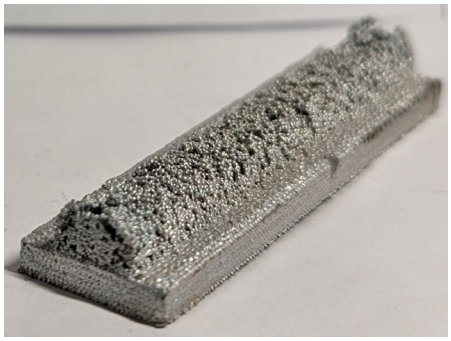

Figure 20. Sample 13: Wick PHT 0.095 ms, Jetting Frequency: 30%, Print Optimization: Off, Infill Type: Shell.

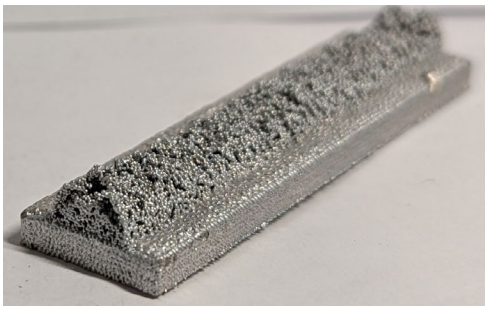

Figure 21. Sample 14: Wick PHT 0.090 ms, Jetting Frequency: 30%, Print Optimization: Off, Infill Type: Shell.

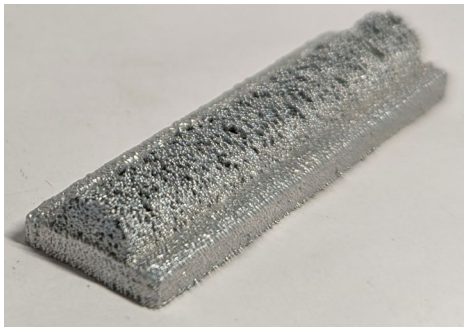

Figure 22. Sample 15: Wick PHT 0.090 ms, Jetting Frequency: 20%, Print Optimization: Off, Infill Type: Shell.

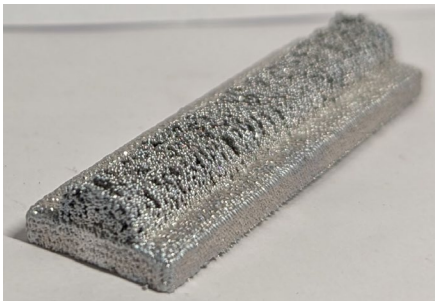

Figure 23. Sample 16: Wick PHT 0.092 ms, Jetting Frequency: 20%, Print Optimization: Off, Infill Type: Shell.

Samples 11–16 all provided passable parts, with a relatively consistent height throughout the entire print. From this, we determined that the optimal range lay somewhere between a PHT of 0.090-0.100 ms, and a JF between 10–30% for the wick. The infill setting that provided the most favorable appearance, at least on the outside, was

a perimeter shell infill. However, further investigation was needed to ensure nothing was compromised for the internal structure.

The different samples are compiled in Table 2, with the samples listed in the order that they were printed and distinguished from one another based on the settings used. Porosity was estimated using the following equation, adapted from [16]:

$$\psi = 1 - \frac{m_s}{\rho_s V},$$

where ψ is the porosity percentage, m_s is the mass of the wick, ρ_s is the density of Al-4008, and V is the volume of the wick. Mass of the wick was measured by subtracting the mass of a base printed without a wick from the total mass of the sample. Since the uneven nature of the samples presented an issue when attempting to calculate the dimensions, the height of the samples was measured at five different points and averaged. The volume was then calculated using the following equation:

$$V = (H_r * W) + (\frac{\pi * (H - H_r) * W}{4}) * L,$$

where H is the height of the wick, W is the width of the wick, L is the length of the wick, and H_r is the Percent Height Retained.

Table 2. Print Samples

#	Wick PHT (ms)	Jetting Freq. (%)	Print Op.	Infill Type	Approximate Porosity (%)	Height Retained (%)
1	0.100	100	Off	Standard	44.50	52.22
2	0.100	100	On	Standard	38.61	64.89
3	0.125-0.100	100	Off	Standard	3.13	62.18
4	0.115	100	Off	Standard	5.70	64.8
5	0.090	100	On	Standard	44.79	44.31

#	Wick PHT (ms)	Jetting Freq. (%)	Print Op.	Infill Type	Approximate Porosity (%)	Height Retained (%)
6	0.095	100	On	Standard	23.61	55.87
7	0.095	10	Off	Standard	31.02	54.18
8	0.095	10	Off	Shell	49.68	53.29
9	0.085	40	Off	Shell	4.58	39.20
10	0.100	40	Off	Shell	5.83	37.33
11	0.100	20	Off	Shell	18.30	63.42
12	0.095	20	Off	Shell	31.62	57.02
13	0.095	30	Off	Shell	31.31	47.24
14	0.090	30	Off	Shell	36.44	36.71
15	0.090	20	Off	Shell	41.52	43.87
16	0.092	20	Off	Shell	42.64	42.09

1. Internal Features

From the first group of samples, we determined the settings that provided the best results were a PHT between 0.100 and 0.090 ms, with a JF between 10% and 30%. Shell-type infills also seemed to help with maintaining proper geometry.

The next step was then to produce several samples within that variation and compare the interior structure to note the effects of changing settings. Figures 24–26 depict the samples printed at a PHT of 0.100 ms, with a side-by side comparison depicting the difference between using the standard infill and the perimeter shell infill. We see that porosity is quite low for all the instances that used the standard infill. Pores are concentrated near the edges of the sample, and towards the center, the part becomes more solid. For the perimeter shell infill, we can see a more obvious trend where the parts become more porous as the JF decreases. Internal porosity is more evenly distributed as well.

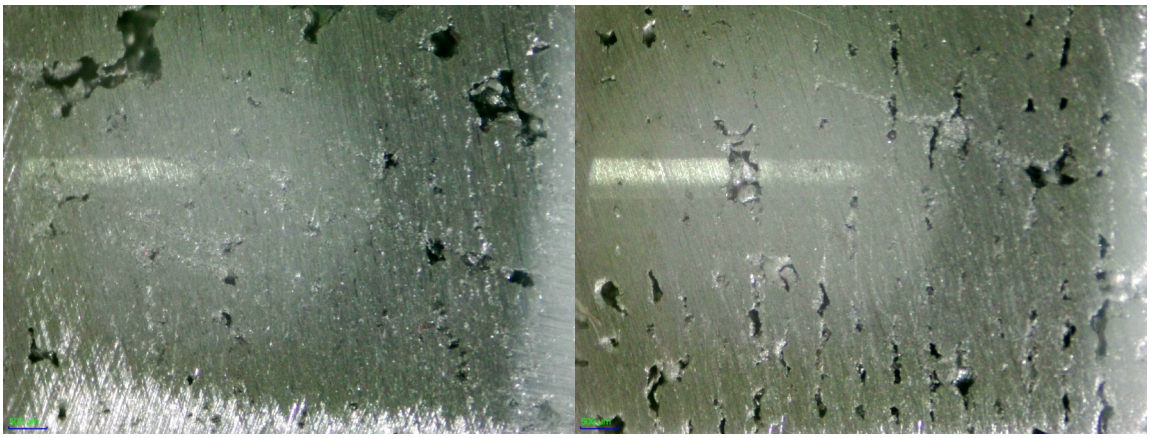

Figure 24. Cross-sections 1–2: PHT 0.100 ms, JF 30%. Standard Infill (Left) and Shell Infill (Right).

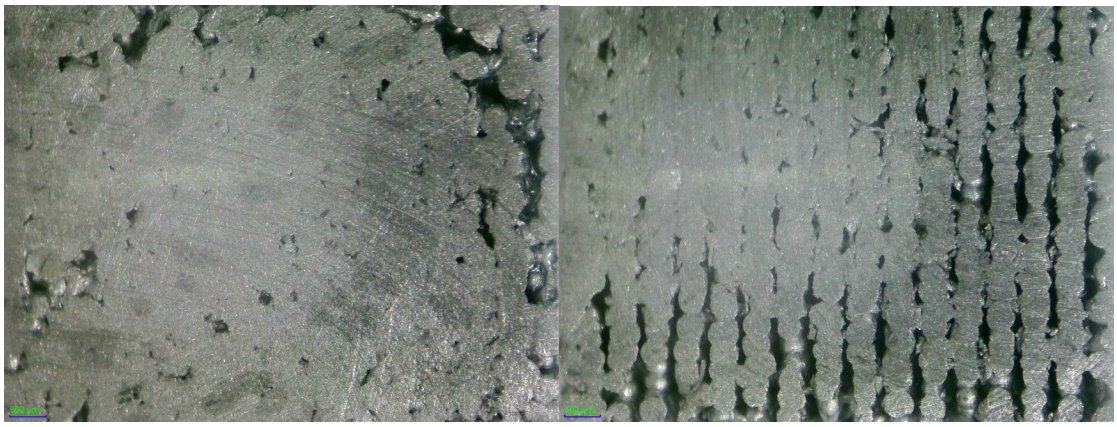

Figure 25. Cross-sections 3–4: PHT 0.100 ms, JF 20%. Standard Infill (Left) and Shell Infill (Right).

Figure 26. Cross-sections 5–6: PHT 0.100 ms, JF 10%. Standard Infill (Left) and Shell Infill (Right).

Figures 27–29 depict the samples printed with a PHT of 0.095 ms. We can see an increase in porosity for both the standard and perimeter shell infills as the JF is decreased. At a JF of 30%, there is barely any porosity in the standard infill. At lower frequencies, the porosity not only increases, but is also more evenly distributed, though the pores seem to still concentrate around the edges. For the shell infill, while we see the increase in porosity with a lower JF, we also start to see an interesting phenomenon in Cross-section Sample 12 at 10% JF. A large gap was left between the outer perimeter and the rest of the infill, showing a lack of cohesion between some of the shells.

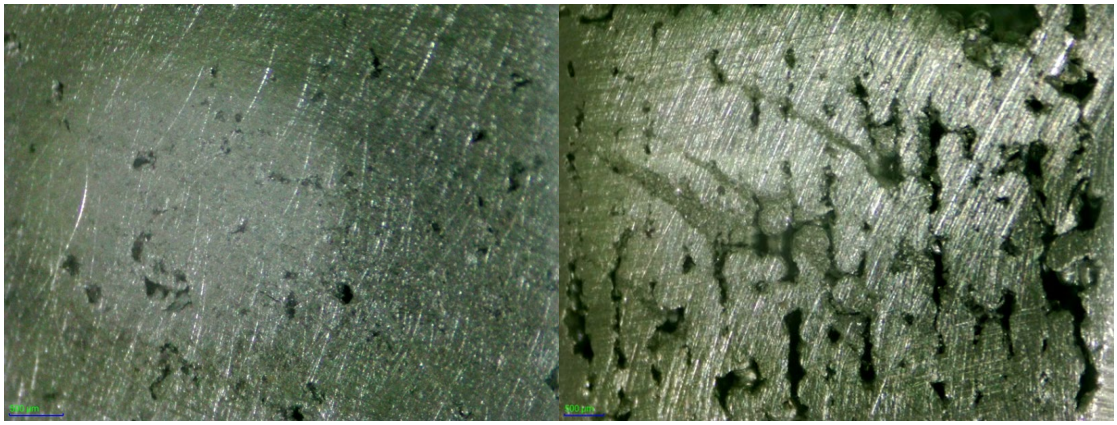

Figure 27. Cross-sections 7–8: PHT 0.095 ms, JF 30%. Standard Infill (Left) and Shell Infill (Right).

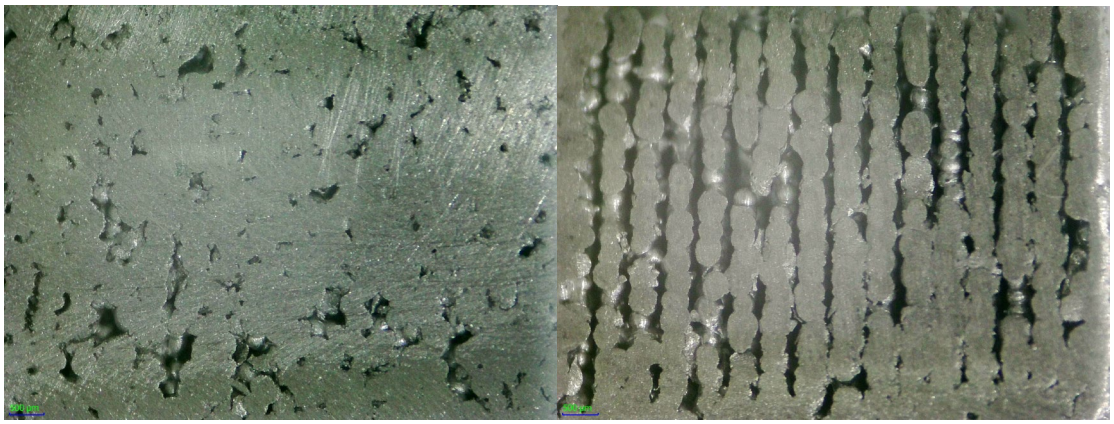

Figure 28. Cross-sections 9–10: PHT 0.095 ms, JF 20%. Standard Infill (Left) and Shell Infill (Right).

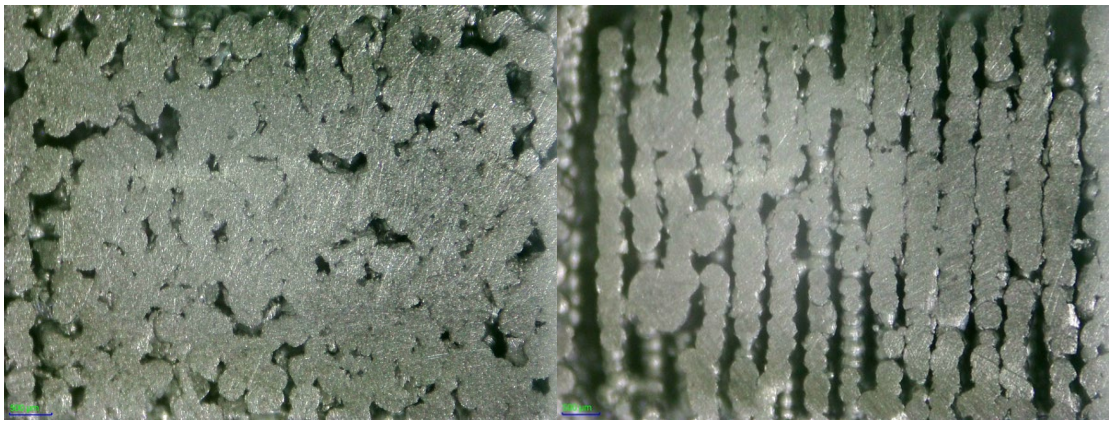

Figure 29. Cross-sections 11–12: PHT 0.095 ms, JF 10%. Standard Infill (Left) and Shell Infill (Right).

Figures 30–32 depict the samples printed with a PHT of 0.090 ms. We start to see a bit of a reversal for the standard infill, where it starts off much more evenly porous, but as the JF is decreased it becomes concentrated at the edges again. A similar occurrence happens with the shell infills between JF 30% and 20% for Cross-section Samples 14 and 16, but at 10% JF we see a more extreme version of what occurred for Cross-section Sample 12. None of the inner shells for Cross-section Sample 18 have properly fused, leaving a series of concentric rectangular walls barely kept together with friction. This became more obvious when the part was cut to observe the cross-section, as the layers then splayed out like book pages, as seen in Figure 33.

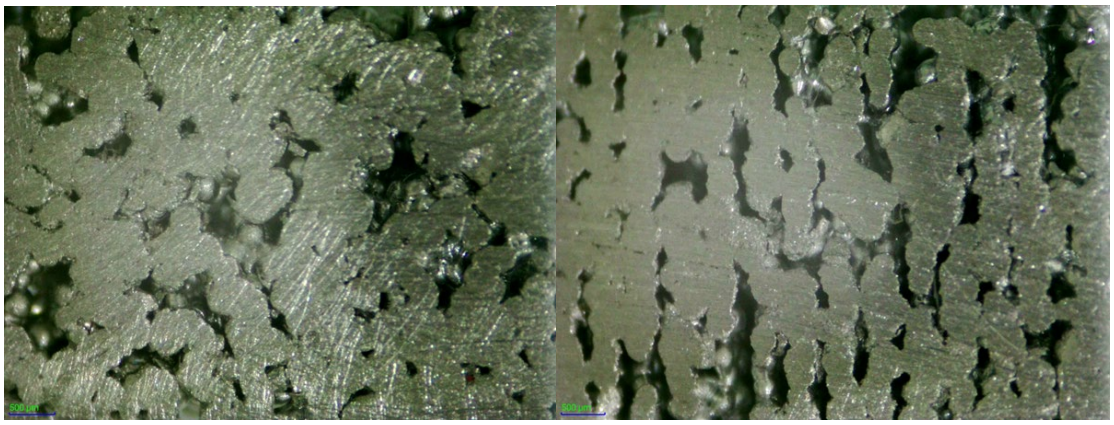

Figure 30. Cross-sections 13–14: PHT 0.090 ms, JF 30%. Standard Infill (Left) and Shell Infill (Right).

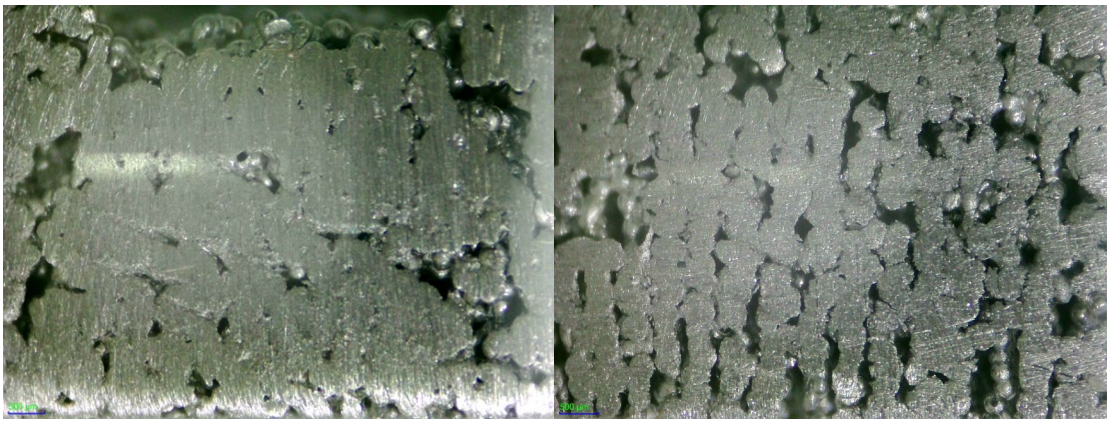

Figure 31. Cross-sections 15–16: PHT 0.090 ms, JF 20%. Standard Infill (Left) and Shell Infill (Right).

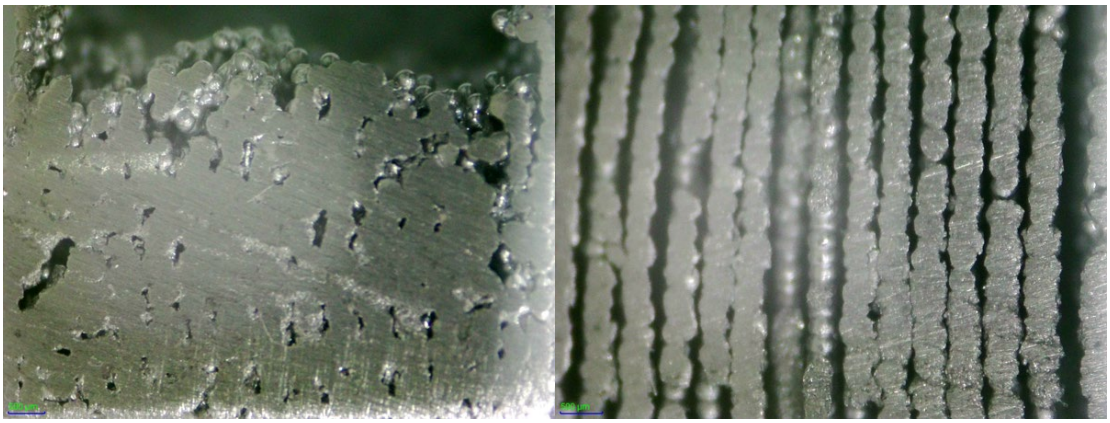

Figure 32. Cross-sections 17–18: PHT 0.090 ms, JF 10%. Standard Infill (Left) and Shell Infill (Right).

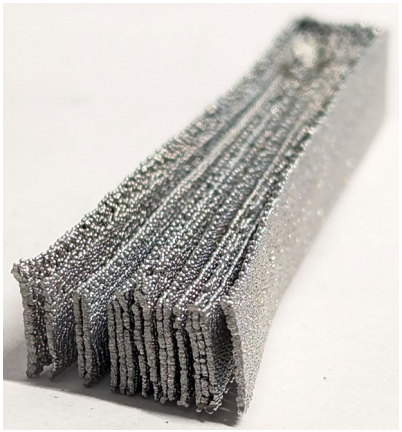

Figure 33. Cross-section: PHT 0.090 ms, JF 10%, Shell Infill.

The porosity of all 18 cross-sections were approximated through grid estimation techniques, then cataloged in Table 3. The cross-sections provide some insight into the level of porosity one could expect throughout the samples. A general trend can be seen where shell-type infills are more porous than standard-type infills using the same settings, but each PHT has a different interaction with decreasing JF.

Table 3. Cross-Sectional Analysis

Sample #	PHT (ms)	JF (%)	Infill Type	Cross-section Porosity (%)
1	0.100	30	Standard	5.58
2	0.100	30	Shell	8.30
3	0.100	20	Standard	8.15
4	0.100	20	Shell	18.30
5	0.100	10	Standard	6.38
6	0.100	10	Shell	31.15
7	0.095	30	Standard	2.85
8	0.095	30	Shell	17.75
9	0.095	20	Standard	13.20
10	0.095	20	Shell	29.38
11	0.095	10	Standard	16.80
12	0.095	10	Shell	30.50
13	0.090	30	Standard	20.70
14	0.090	30	Shell	27.18
15	0.090	20	Standard	12.75
16	0.090	20	Shell	20.63
17	0.090	10	Standard	13.53
18	0.090	10	Shell	31.75

2. Alternative Designs

In addition to the designs used for the samples, alternate models were made as possible designs, based on the constraints of the ElemX printer. The model had pillars designed into the CAD model, since generating internal supports through the slicer would not be possible. Despite the attempt at compensating for the lack of supports, Figure 34 shows that while the design needed more fine-tuning to avoid having the roof of the part collapse, the theory behind it has some merit.

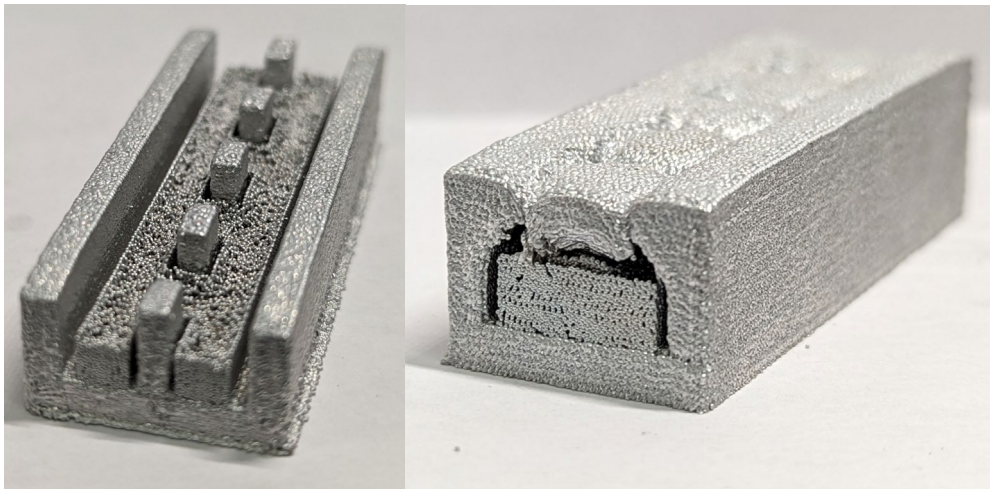

Figure 34. Alternate Design: Heat Pipe with Internal Support.

3. Issues, Faults, and Other Sources of Error

Some notable sources of error were present during the printing process. When beginning a new print, the lower PHT and JF settings meant that the pre-programmed settings for the height of the print head no longer provided the proper height for the size of the drop mass. If the print head were too high, the particles would solidify before they hit the build plate and bounce off. If the print head were too low, the particles would attach too strongly to the build plate and make it difficult to remove. Since the porous objects had brittle properties, prints would sometimes suffer breaks when half of the object was strongly attached to the plate and the other half was freed from the plate.

One of the most common issues that appeared during the printing process came from either clogged or faulty nozzles. When printing at a low jetting frequency along with low PHTs, the nozzle will occasionally stop jetting material in the middle of the print while the print bed continues to move as programmed. One possible reason is that the nozzle itself is not heated, so it relies on the transferred heat from the jetted particles to reach an acceptable temperature. Smaller particles that are passing through at a lower rate do not transfer enough heat to the nozzle, causing some to solidify before deposition and eventually causing a blockage. The issue can be resolved by adjusting the PHT to a higher amount, but any layers that were in progress during the fix would be lost. In cases of severe blockages that are not caught in time, it can also cause molten metal to pool at the nozzle before falling as large beads of aluminum like they do in Figure 35.

Figure 35. Large Beads of Aluminum.

In addition to continuity errors, additional problems can occur when a nozzle no longer jets metal in a straight path. This is most evident if the printer has been running for

a long time or has been left idle too long. If the metal jets at an angle or as a spray instead of a vertical stream, it can cause a loss in print quality. Even objects printed at the recommended settings can be rendered coarse or uneven if the nozzle is in this state. This becomes even more evident in cases like the one shown in Figure 36, where two objects have been printed using the same settings but have drastically different print quality.

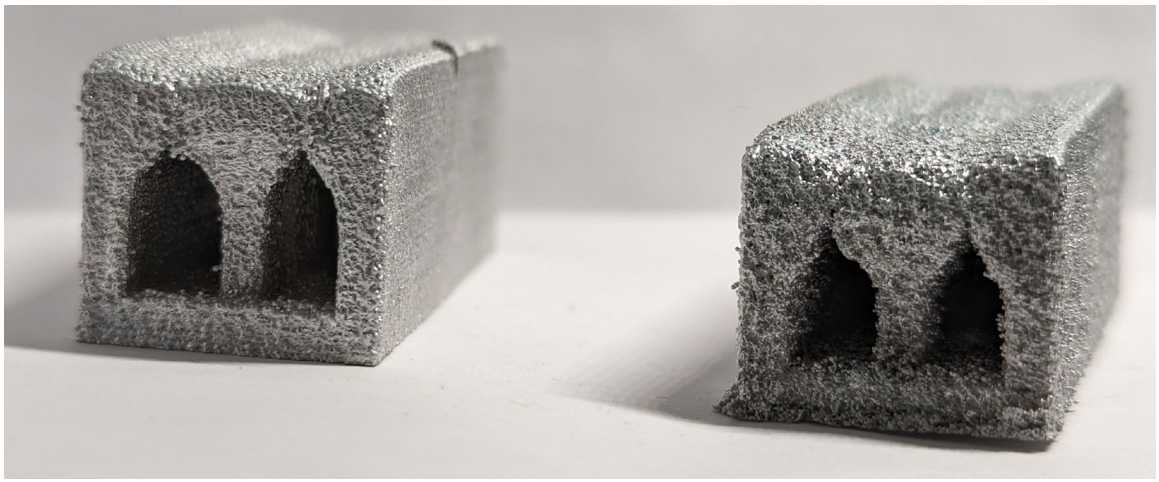

Figure 36. Two Objects Printed with the Same Settings with Different Nozzles.

Objects printed at lower settings usually have uneven top layers. While in general the peaks and valleys are randomly generated, the most notable peaks are concentrated in spots where the print bed changes direction for a corner or new layer. While there appears to be some settings on the ElemX slicer program meant to aid with such issues, the use of the setting is not listed in the provided guidebook.

B. FLUID TESTING

While the previous tests proved that the structures had some level of porosity, it does not guarantee that a continuous path of pores existed throughout the structure. To determine whether it can properly transport fluid, another part was designed by extruding the CAD model used in Part A into a U-shape. A series of the U-Shaped parts were then printed with wicks made with some of the more promising settings.

Using this new part, a test was conducted using the set-up portrayed in Figure 37. The wick of the part was saturated with water and then placed with one end submerged in a beaker of water at a depth of 15 mm while the other hung freely over the side of the beaker above a collection container. The part was then allowed to drip until the drops reached a steady rate of flow. Once a steady state had been reached, a five-minute timer was started following the fall of another drop. The collection container was then removed, and a petri dish was placed underneath the free end of the part. After five minutes, the petri dish was removed and any water still in the process of falling from the end of the part was collected into the dish. The petri dish was then weighed on a scale that had already been calibrated to account for the weight of the dish, and the mass was recorded. The process was then repeated for the remaining printed structures.

Figure 37. Wick Fluid Test.

Figures 38–43 depict the six U-shaped designs used. The results of the experiment are documented in Table 4, calculated from the mass of the collected water divided by the five minutes for the test.

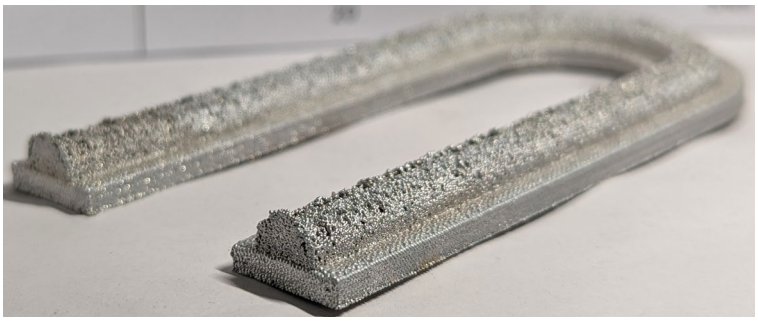

Figure 38. U-Shaped Design 1 (PHT: 0.100 ms, JF: 20%, Shell Infill).

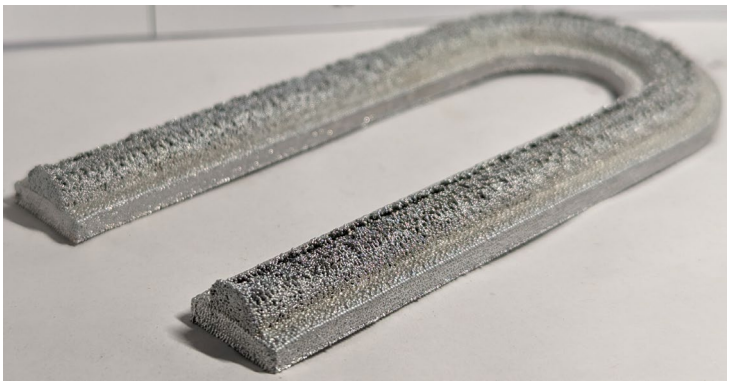

Figure 39. U-Shaped Design 2 (PHT: 0.095 ms, JF: 20%, Standard Infill).

Figure 40. U-Shaped Design 3 (PHT: 0.095 ms, JF: 20%, Shell Infill).

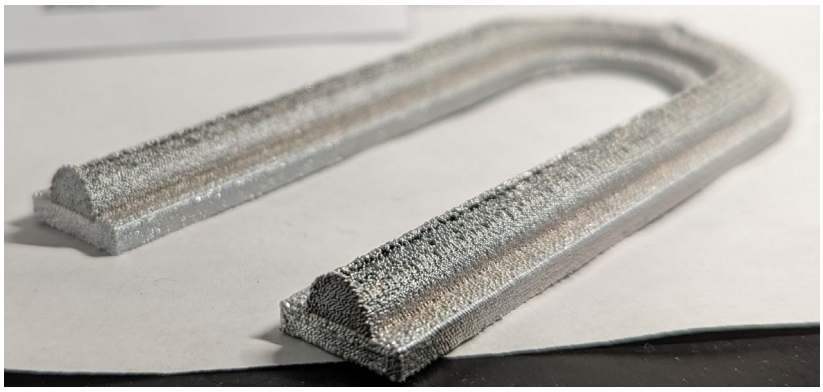

Figure 41. U-Shaped Design 4 (PHT: 0.095 ms, JF: 10%, Shell Infill).

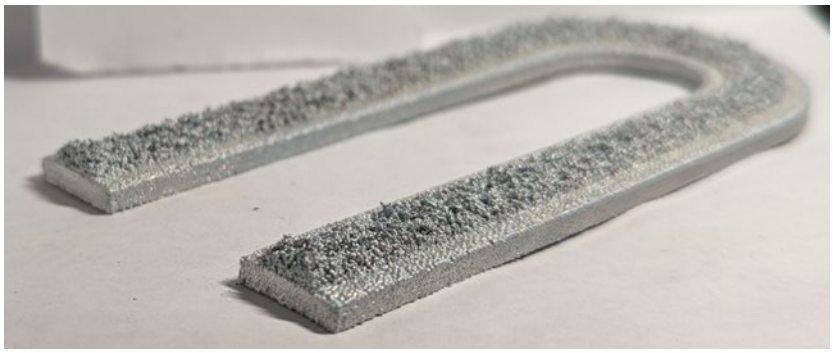

Figure 42. U-Shaped Design 5 (PHT: 0.090 ms, JF: 30%, Shell Infill).

Figure 43. U-Shaped Design 6 (PHT: 0.090 ms, JF: 20%, Shell Infill).

Designs 1, 2, 3, 4, and 6 were successfully able to transport water. While Design 5 initially retained water, it was not able to continue a steady drop rate of water, which could be due to either a lack of continuous porosity, or because the smaller cross-sectional surface area meant that it was not able to provide the necessary capillary head force to draw in more fluid. The design that performed the best was Design 3, which was

printed at a PHT of 0.095 ms, JF of 20%, and a perimeter shell infill. This is consistent with the level of porosity observed in the cross-section test, and comparable to the flow rates seen in some other heat pipe wick tests that had a liquid flow rate of about 0.18-0.4 g/min for water through a homogenous wick [17].

As the wick is open to the air, we can assume atmospheric temperature for the top of the wick, while the submerged end is at 147.15 Pa. We can assume a density of 1000 kg/m^3 for water and a gravitational constant of 9.81 m/s^2.

Table 4. Mass Flow Rate

#	Wick PHT (ms)	Jetting Freq. (%)	Infill Type	Mass Flow Rate (g/min)
1	0.100	20	Shell	0.0858
2	0.095	20	Standard	0.0292
3	0.095	20	Shell	0.4734
4	0.095	10	Shell	0.1502
5	0.090	30	Shell	N/A
6	0.090	20	Shell	0.1702

As the issues for Design 5 could be due to loss in height, the CAD model of the wick was altered to attempt to compensate for the expected shrinkage. The new design was able to effectively transport water, but only at a rate of 0.0424 g/min, which was much slower than any of the other samples.

C. STRENGTH TESTING

To evaluate the difference in strength that arose from the changes in parameters, several beams were printed to observe how the physical properties changed. The model was designed as a solid 8x14x50 rectangular beam. Two beams were printed at a PHT of 0.130 ms and a JF of 100%. The first was designed with a standard infill, while the other

had a perimeter shell infill, to test for any potential differences between one over the other. Another model was designed as a solid 16x14x50 rectangular beam, to compensate for the height loss expected from printing at lower settings. Two beams were printed at a PHT of 0.095 ms and a JF of 20% to simulate the strength of just the wick. In addition, there was a sample "heat pipe" using an extruded version of the original sample with an additional upper cover, shown in Figure 44. This sample was used to see the layer interaction between a composite part.

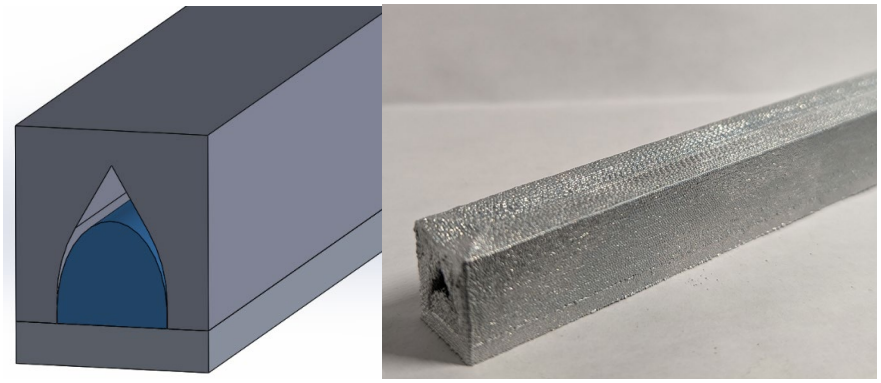

Figure 44. Covered Heat Pipe Design. CAD Design (Left), Printed Model (Right).

The beams were tested in an Instron Bend Fixture Series using a 3-Point flexure method, shown in Figure 45. The beams are supported by a roller at each end, separated by 110 mm. A third roller applied a downward force at the center of the beams, proceeding at a speed of 2 mm per minute. The machine measured the applied force, time elapsed, and total displacement of the top roller, and exported the information in a table format.

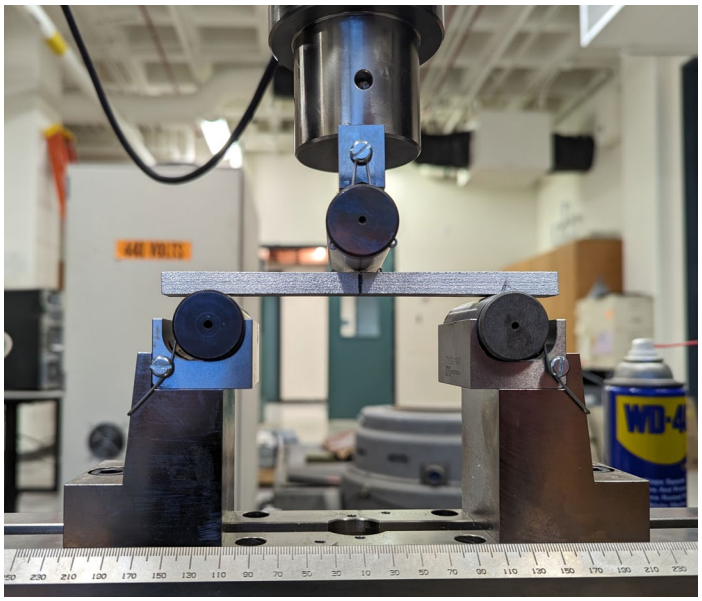

Figure 45. Three-Point Bend Fixture Setup.

Both samples printed at the recommended settings exhibited ductile failure, becoming permanently deformed without fracturing. A graph was made using the exported data, shown in Figure 46, indicating the beams experienced a maximum stress before yield. The corresponding data points reveal that the maximum force applied before yielding for the standard infill was 1.582 kN, while for the shell infill, the maximum force was 1.506 kN. Flexural stress was calculated using the following formula [18]:

$$\sigma_f = \frac{FL}{bd^2},$$

where F is the force applied to the center in Newtons, L is the distance in mm between the two points of contact at the bottom of the beam, b is the width of the beam in mm, and d is the depth or thickness in mm.

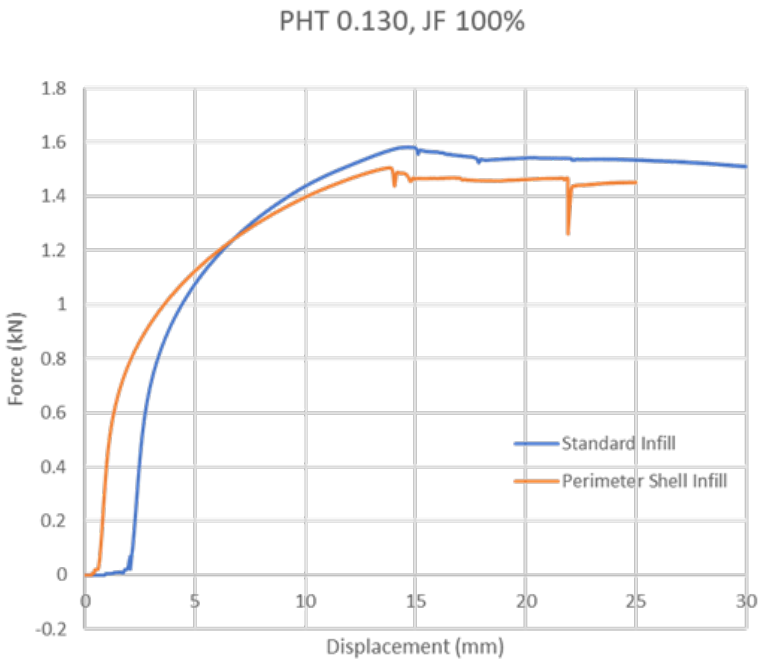

Figure 46. Graphic Comparison of Shell vs. Perimeter Shell Infill at Recommended Setting (PHT: 0.130 ms, JF: 100%).

Some of the difference comes from a size difference, as the standard infill resulted in a part that was on average 0.68 mm taller. In terms of yield stress, the shell infill had a higher value at 180.66 MPa, compared to the 161.20 MPa of the standard infill. These are smaller compared to other reported yield stress values of other samples made from 3D printed aluminum, which range from 300–340 MPa [19], though it is important to note that the samples were not heat treated as the others were.

At lower settings (PHT 0.095 ms, JF 20%), the experiment yielded results resembling a brittle failure, depicted in Figure 47. The beams experienced some deformation before undergoing a fracture originating opposite of the applied force and growing as more force was applied over time. However, as shown in the graph in Figure 48, the shell infill fracture was not as abrupt as it was for the standard infill, which could indicate that the rupture was a series of ductile failures on the microscopic level which then gave the appearance of a brittle fracture on the macroscopic scale.

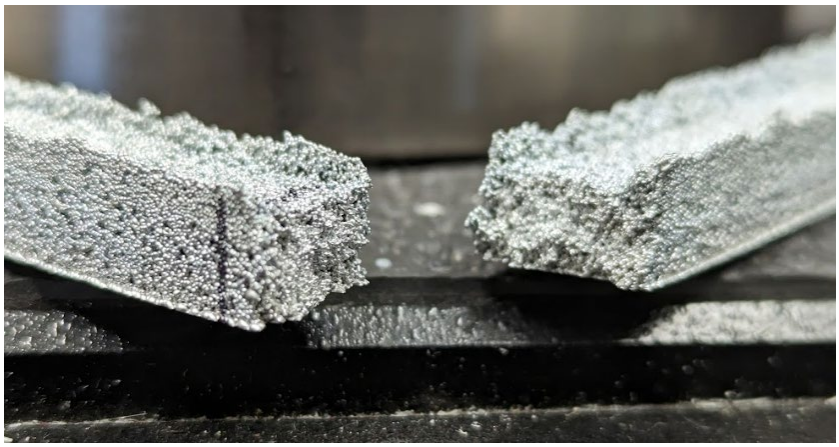

Figure 47. Brittle Fracture (PHT: 0.095 ms, JF: 20%, Standard Infill).

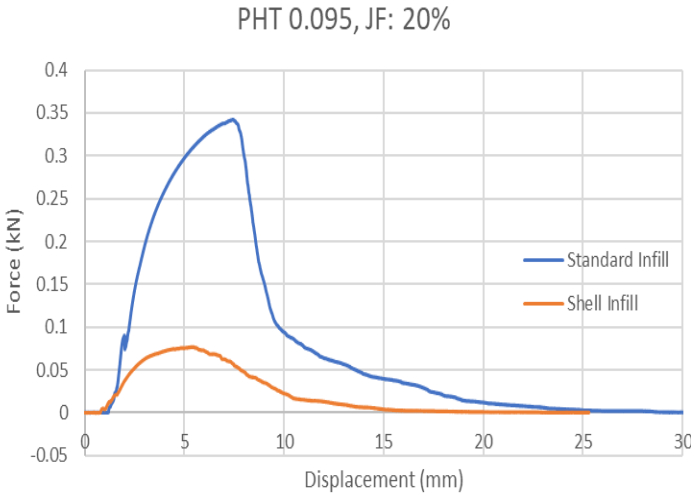

Figure 48. Graphic Comparison of Shell vs. Perimeter Infill for Wick Samples (PHT: 0.095 ms, JF: 20%).

The standard infill provided a sample that withstood 0.342 kN, while the shell infill only made it to 0.078 kN before failure. This corresponds to an apparent yield stress of 47.5 MPa and 10.75 MPa, respectively. These need to be corrected based on the porosity values, as the actual contact area would be much less for the shell infill than it would be for the standard infill. In addition, stress concentration at droplet interfaces would reduce ductility, as cracks form more easily. More samples need to be tested to provide a better comparison and to ensure repeatable results.

For the composite structure, there is a combination of factors at play. Along with the porous structure that had been printed over the base layer, the top cover also created a point of separation, as it had to be printed after the wick. Due to the improper fusion of the top cover to the base layer, a split can be seen between the layers in Figure 49 as it was in the process of fracturing.

Figure 49. Layer Splitting on Composite Beam.

A maximum force was 7.76 kN was achieved, and in Figure 50 we see that the division in the composite structure may have caused the graph to change its slope by the 17 mm mark. The maximum stress was calculated using the equations for flexural stress in a non-homogenous beam, adapted from [20] and the equation for 3-point loading used in the previous tests:

$$\sigma = \frac{-FLE_1 c_1}{4\overline{EI}},$$

where F is the force applied in N, L is the distance between the points in mm, E is the elastic modulus of the part, c is distance from the centroid of the part to the centroid of the structure in mm, and $\overline{EI}$ is the Weighted Flexural Rigidity. Utilizing the dimensions of the beam and the moment of inertia for each part calculated in SolidWorks, we estimated the maximum stress to be about 289.8 MPa at the bottom of the beam, though factors such as the porosity of the wick may also need to be considered.

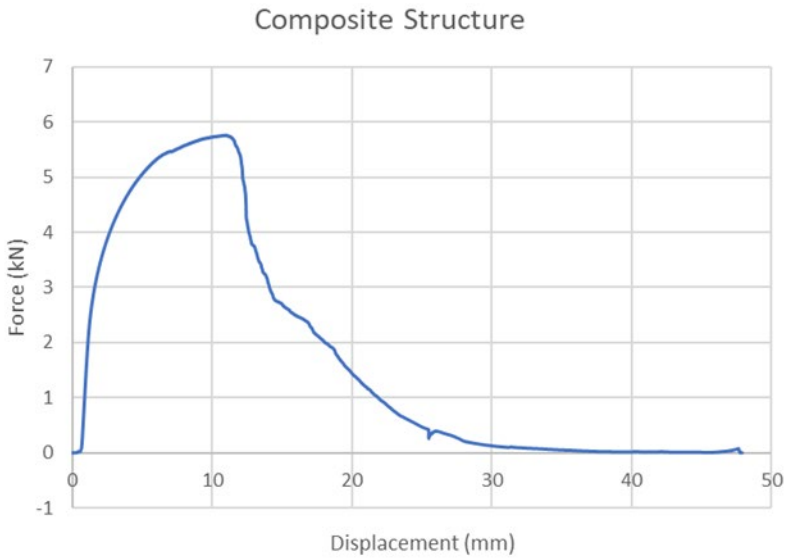

Figure 50. Graph of Composite Structure, (PHT: 0.095 ms, JF: 20%)

THIS PAGE INTENTIONALLY LEFT BLANK

IV. CONCLUSIONS AND FUTURE WORK

The procedures conducted proved that by altering the settings, a continuously porous structure could be printed that is capable of capillary action. In addition, it showed that a part with multiple densities could be made, whether by altering the settings mid-print or by printing directly on a previous print. Flexural testing revealed that the porous structures reacted as though they were brittle when subjected to loading, contrary to the ductile deformation that usually occurs with Aluminum.

The preferences that provided the most promising results came from using a PHT between 0.090-0.100 ms and a jetting frequency of 20%. Using a PHT of less than 0.090 ms results in too much loss in volume, while greater than 0.100 ms has too much loss in porosity. Using a jetting frequency of 10% allows for a greater retention of shape, but the slower speed results in less reliability for larger parts as the nozzle tends to jam when a low JF is used in conjunction with lower PHTs.

When slicing the 3D model, the method of infill played a significant role in how the inner structure would look like. By far, the most consistently porous structures came from models created using a perimeter shell infill. Meanwhile, the standard infill often resulted in cross-sections that were porous along the edges of the structure, but solid in the middle. From the cross-section observations, the maximum porosity achieved was about 32% porosity per cross-sectional area, which is approximately 48% porosity by volume.

The fluid testing showed that a wick with a PHT of 0.095 ms, JF of 20%, and a shell infill works best, being able to transport 0.4734 g/min of water. Other wick geometries have produced mixed results, with height loss playing a factor in the amount of water able to be retained. Strength testing of the composite hollow structure with a solid aluminum shell and a porous wick able showed it to be able to withstand flexural stresses of up to 225.97 MPa before failure.

Future testing would involve assessing the heat transfer capabilities of the heat pipes printed with the ElemX Printer, as well as other porous structures. As this research focused on the structural aspects, experimentation with working fluids did not occur.

While the limitations of the ElemX printer would prevent printing a circular circumferential heat pipe, there are some ways to fabricate various kinds of heat pipes. The ones that the team focused on for the current project were unidirectional heat pipes, but it should be possible to achieve a circumferential wick by experimenting with the angle limitations at the lower settings. Alternatively, it may be printed in pieces and put together afterwards, attaching the pieces either through welding or through printing directly on the parts to join them together like in Figure 51.

Figure 51. Potential Circumferential Heat Pipe Design.

LIST OF REFERENCES

[1] *Department of Defense Additive Manufacturing Strategy*, DOPSR case #21-S-0711, Office of the Deputy Director for Strategic Technology Protection and Exploitation, Washington, DC, USA, Jan. 2021. Available: https://www.cto.mil/wp-content/uploads/2021/01/dod-additive-manufacturing-strategy.pdf

[2] V. Wang, "Stochastic low density liquid metal printing," M.S. thesis, MAE Dept., Naval Postgraduate School, Monterey, CA, 2023.

[3] D. Reay, R. McGlen, and P. Kew, *Heat Pipes: Theory, Design and Applications*. Burlington, MA, USA: Elsevier Science & Technology, 2006. Available: http://ebookcentral.proquest.com/lib/ebook-nps/detail.action?docID=274682

[4] S. Farooqi, "One drop at a time: Xerox 3D prints with liquid metal," Engineering.com, Feb. 11, 2021. Available: https://www.engineering.com/story/one-drop-at-a-time-xerox-3d-prints-with-liquid-metal

[5] Xerox ElemX 3D Printer Operator Manual, v1.2, Xerox. 2021.

[6] N. Zheng, Z. Liu, Y. Pang, F. Cai, and S. Zhao, "Study on flow and heat transfer characteristics of 3D molten aluminum droplet printing process," *International Journal of Heat and Mass Transfer*, vol. 204, p. 123863, May 2023. Available: doi: 10.1016/j.ijheatmasstransfer.2023.123863.

[7] Xerox ElemX 3D Printer Design Guide, v1.0, Xerox. 2021.

[8] "United States Welding Corporation," Al-4008 (A356). Accessed: Nov. 6, 2023 [Online]. Available: https://www.usweldingcorp.net/TDS/tds4181.pdf

[9] C. Fletcher, "Metallography guide for Xerox® 4008 aluminum wire," Xerox, Jan. 2022. Available: https://www.xerox.com/downloads/usa/en/3d-printing/ElemX-Metallography-Guide.pdf

[10] J. Ku, "Introduction to heat pipes – NASA," presented at the *Thermal & Fluids Analysis Workshop*, NASA/Goddard Space Flight Center, 2015. Available: https://tfaws.nasa.gov/wp-content/uploads/TFAWS2015-SC-Heat-Pipes.pdf

[11] D. Grabaskas, "Heat-Pipe Microreactors," presented at the *Fast Reactor Technology Training*, Argonne National Laboratory, Mar. 27, 2019. Available: https://www.nrc.gov/docs/ML1915/ML19150A609.pdf

[12] A. Faghri, "Review and advances in heat pipe science and technology," *Journal of Heat Transfer*, vol. 134, no. 123001, Oct. 2012. Available: doi: 10.1115/1.4007407.

[13] Y. Luo et al., "Modeling and experimental analysis of U-shaped segmented unidirectional heat pipe array cogeneration unit," *Case Studies in Thermal Engineering*, vol. 26, p. 101074, Aug. 2021. Available: doi: 10.1016/j.csite.2021.101074.

[14] C. Chang, Z. Han, X. He, Z. Wang, and Y. Ji, "3D printed aluminum flat heat pipes with micro grooves for efficient thermal management of high power LEDs," *Sci Rep*, vol. 11, no. 1, Art. no. 1, Apr. 2021. Available: doi: 10.1038/s41598-021-87798-4.

[15] B. Lin, R. Xie, and L. Tao, "Study of the heat transfer performance of a loop heat pipe with aluminum wick," *Thermal Science*, vol. 26, pp. 248–248, Jan. 2021. Available: doi: 10.2298/TSCI200904248L.

[16] J. Zhang, L. Lian, Y. Liu, and R. Wang, "The heat transfer capability prediction of heat pipes based on capillary rise test of wicks," *International Journal of Heat and Mass Transfer*, vol. 164, p. 120536, Jan. 2021. Available: doi: 10.1016/j.ijheatmasstransfer.2020.120536.

[17] L. R. Wermer et al., "A high-capacity self-priming counter-gravity heat pipe: Modeling and experimental demonstration," *International Journal of Heat and Mass Transfer*, vol. 125, pp. 1369–1378, Oct. 2018. Available: doi: 10.1016/j.ijheatmasstransfer.2018.04.161.

[18] I. Westermann, K. E. Snilsberg, Z. Sharifi, O. S. Hopperstad, K. Marthinsen, and B. Holmedal, "Three-point bending of heat-treatable aluminum alloys: Influence of microstructure and texture on bendability and fracture behavior," *Metallurgic and Material Transactions A*, vol. 42, no. 11, pp. 3386–3398, Nov. 2011. Available: doi: 10.1007/s11661-011-0768-y.

[19] A. Elliott, A. Shyam, O. Rios, and T. Muth, "Advancing liquid metal jet printing," Oak Ridge National Laboratory, Oak Ridge, TN, USA. CRADA/ NFE-18-07178, Sep. 2019. Available: https://www.ornl.gov/sites/default/files/2019-10/Vader%20Systems%20Final%20Report.pdf

[20] R. R. Craig, *Mechanics of materials*, 3rd ed. Hoboken, NJ, USA: Wiley, 2011.

INITIAL DISTRIBUTION LIST

1. Defense Technical Information Center
   Fort Belvoir, Virginia

2. Dudley Knox Library
   Naval Postgraduate School
   Monterey, California